JACS
JOURNAL OF THE AMERICAN CHEMICAL SOCIETY
Article
pubs.acs.org/JACS

Instantaneous Generation of Charge-Separated State on TiO_2 Surface Sensitized with Plasmonic Nanoparticles

Run Long[‡,§] and Oleg V Prezhdo*[,§]

[‡]School of Physics and Complex & Adaptive Systems Laboratory, University College Dublin, Dublin, Ireland
[§]Department of Chemistry, University of Rochester, Rochester, New York 14627, United States

Supporting Information

ABSTRACT: Photoexcitation of the plasmon band in metallic nanoparticles adsorbed on a TiO_2 surface initiates many important photovoltaic and photocatalytic processes. The traditional view on the photoinduced charge separation involves excitation of a surface plasmon, its subsequent dephasing into electron−hole pairs, followed by electron transfer (ET) from the metal nanoparticle into TiO_2. We use nonadiabatic molecular dynamics combined with time-domain density functional theory to demonstrate that an electron appears inside TiO_2 immediately upon photoexcitation with a high probability (∼50%), bypassing the intermediate step of electron−hole thermalization inside the nanoparticle. By providing a detailed, atomistic description of the charge separation, energy relaxation, and electron−hole recombination processes, the simulation rationalizes why the experimentally observed ultrafast photoinduced ET in an Au−TiO_2 system is possible in spite of the fast energy relaxation. The simulation shows that the photogenerated plasmon is highly delocalized onto TiO_2, and thus, it is shared by the electron donor and acceptor materials. In the 50% of the cases remaining after the instantaneous photogeneration of the charge-separated state, the electron injects into TiO_2 on a sub-100 fs time scale by the nonadiabatic mechanism due to high density of acceptor states. The electron−phonon relaxation parallels the injection and is slower, resulting in a transient heating of the TiO_2 surface by 40 K. Driven by entropy, the electron moves further into TiO_2 bulk. If the electron remains trapped at the TiO_2 surface, it recombines with the hole on a picosecond time scale. The obtained ET and recombination times are in excellent agreement with the experiment. The delocalized plasmon state observed in our study establishes a novel concept for plasmonic photosensitization of wide band gap semiconductors, leading to efficient conversion of photons to charge carriers and to hybrid materials with a wide variety of applications in photocatalysis and photovoltaics.

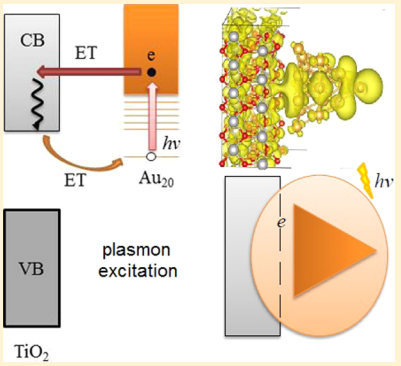

1. INTRODUCTION

The prominent catalytic properties of gold nanoparticles on well-ordered metal oxide substrates[1−4] stimulate extensive research activities. These systems combine the light-harvesting ability of semiconductor nanocrystals[5] with the catalytic activity of small metal particles,[6] showing great promise in photocatalysis, such as light-driven hydrogen production.[7−9] Interfacial electron transfer (ET)[10] is key to light-induced activity, because the latter depends on the ability of a catalyst to create and efficiently separate electron−hole pairs. The photoinduced electron−hole separation facilitates redox reactions via formation of adsorbed radicals on semiconductor surface. Many factors affect photocatalytic processes, especially those concerning the fate of the carriers that have reached the catalytic surface: do these charges directly react with adsorbates, or are they first trapped by surface species and then transferred to the reactants? High photochemical yields require that the charge generation rate far exceeds the rates of charge relaxation and recombination.

Solar cells based on semiconductor sensitization with metal nanoparticles[1,11−16] have attracted significant attention because of the unique electronic and optical properties of metallic clusters. The exciting optical physics of metal nanoparticles arises from the resonant interaction of conduction band electrons and the electromagnetic field.[17−23] The collective excitations, usually known as plasmons, are responsible for the specific light extinction and high local fields. Surface plasmons are propagating electron density waves occurring at the interface between metal and dielectric. They can be viewed as electromagnetic waves strongly bound to the interface. In particular, the physical origin of the light absorption by metal nanoparticles is the coherent oscillation of the conduction band electrons induced by the electromagnetic field. The oscillation modes that comprise an electromagnetic field coupled to the oscillations of the conduction band electrons are called surface plasmons.[24] Plasmon excitations trigger nontrivial electron−phonon dynamics. In optical, electronic, and photovoltaic devices, electron−phonon coupling causes nonradiative energy loss and system heating and should be avoided. At the same time, rapid electron−vibrational relaxation is key to applications of metal nanoparticles in photothermal therapy, in which the absorbed photon energy is converted into heat.[25−27] Similarly,

Received: January 7, 2014
Published: February 25, 2014

   dx.doi.org/10.1021/ja5001592 | J. Am. Chem. Soc. 2014, 136, 4343−4354

fast electron−phonon relaxation shortens the response time of electro-optic switches.[28]

Gold nanoparticles deposited onto TiO_2 can increase the power-conversion efficiency of the dye-sensitized solar cell. The localized surface-plasmon resonance enhances light absorption of molecular chromophores.[29,30] Alternatively, excitation of the surface plasmon band can be exploited directly, bypassing the need for traditional dyes. Gold nanoparticle−TiO_2 systems exhibit efficient light-to-charge conversion under excitation at the wavelength of the plasmon band.[11,16,31] The gold nanoparticle−TiO_2 composites can overcome the lack of visible light response of TiO_2 and promote TiO_2 photocatalytic activity. Recently, Kilin and co-workers investigated the electron and hole relaxation dynamics at the Au/Si metal-semiconductor nanointerface co-doped by aluminum and phosphorus.[32] In contrast to molecular and semiconductor quantum dot (QD) chromophores, metallic particles exhibit small or zero band gap, allowing for rapid electron−hole recombination. In order to achieve the photovoltaic and photocatalytic activity, the electron injection from the gold nanoparticles into the TiO_2 substrate should be faster than the recombination. These phenomena provide strong motivation for investigation of microscopic details of the charge- and energy-transfer dynamics at the gold nanoparticle−TiO_2 interface.

Figure 1a presents a diagram of the energy levels in a gold nanoparticle−TiO_2 system, while Figure 1b demonstrates the commonly assumed sequence of events. Absorption of a photon by the nanoparticle surface plasmon is particularly strong near the sharp features of the nanoparticle. The collective plasmonic excitation dephases into electron−hole pairs on a sub-10 fs time scale. The holes are substantially lower in energy than the valence band states of TiO_2 and remain inside the particle. (Note that hole energy rises as one proceeds down in energy along the occupied orbital manifold.) The electrons inside the metal particles are in energetic resonance with the TiO_2 conduction band states, and therefore, the electrons are injected into TiO_2. Simultaneously, electrons and holes relax in energy by coupling to vibrational motions of the nanoparticle and TiO_2 atoms. If the electron is able to lose its energy to phonons and recombine with the hole faster than the injection, the absorbed photon energy is lost to heat. The injection leads to a charge-separated state, with the electrons at the bottom of the TiO_2 conduction band and the holes near the gold nanoparticle Fermi level. At this point, the electrons can delocalize into TiO_2 bulk or again recombine with the holes. Once in the bulk, the electrons diffuse inside TiO_2 toward an electrode or a chemical reaction site. If an electron that has already reached the bulk returns to the surface and recombines with the hole, the photon-to-charge conversion yield is reduced. Therefore, it is critical for photovoltaic and photocatalytic applications that charge separation across the metal particle−TiO_2 interface occurs rapidly.

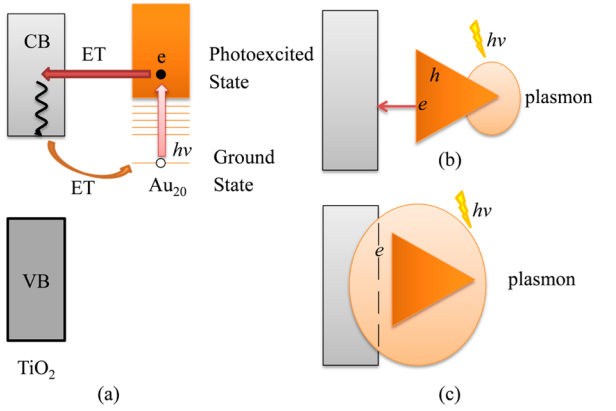

Figure 1. (a) Energy diagram for the photoinduced electron injection, relaxation, and recombination processes. An absorbed photon excites a plasmon in the Au nanocluster. The charge-separated state can be created via two alternative mechanisms. (b) The traditional view assumes that the plasmon breaks into electron−hole pairs, after which an electron is injected into the TiO_2 conduction band. (c) The current study shows that in about 50% of the cases, the electron appears inside TiO_2 immediately upon the plasmon excitation. This is because the plasmon is already delocalized onto TiO_2. The remaining 50% of electrons are injected by the nonadiabatic mechanism. During and after the injection the energy is lost to heat due to coupling to phonons. The study shows that injection proceeds faster than energy losses. Once the electron has relaxed to the bottom of the TiO_2 conduction band, it can return to the nanocluster by recombining with the hole.

Figure 1c demonstrates an alternative mechanism for the photoinduced charge separation in the Au−TiO_2 system. Here, the plasmon excitation exhibits a strong delocalization into TiO_2 surface. As a result, there exists a significant probability for the electron to find itself inside TiO_2 immediately upon the photoexcitation. According to this scenario, the charge-separated state is generated instantaneously. The high density of TiO_2 states ensures that the electron delocalizes into TiO_2 bulk vary rapidly, and the time-scale of the charge-phonon relaxation and electron−hole recombination becomes essentially irrelevant for the photovoltaic and photocatalytic response.

Furube et al. employed a femtosecond transient absorption spectroscopy with an IR probe to report ultrafast extraction of electrons from excited gold nanoparticles into the TiO_2 semiconductor.[11] The extraction occurred within <240 fs, as limited by the experimental time resolution. At the same time, the electron−hole recombination exhibited a broad range of time scales, from 1 ps to nanoseconds. The extremely fast, sub-240 fs, nonequilibrium ET from the gold nanoparticles into the TiO_2 surface makes it difficult to invoke traditional ET models, such as the Marcus theory. The latter makes a quasi-equilibrium assumption, and therefore, it is applicable to sufficiently slow ET, which allow for energy redistribution.

The present work applies the state-of-the-art theoretical technique[33−35] developed in our group and combining time-domain density functional theory (TDDFT) with nonadiabatic molecular dynamics (MD) to investigate the nonequilibrium, plasmon-driven dynamics at the gold nanoparticle−TiO_2 interface. The work of Schatz, Jensen, and Aikens[21] showed how collective plasmon excitations arise in TDDFT from single particle transitions between Kohn−Sham (KS) orbitals, as the size of a metallic particle grows. Individual single-electron transitions form a broad excitation band, matching the plasmon band of metals particles several nanometers in size. Other techniques, such as the electron-driven discrete-dipole approximation (*e*-DDA), developed recently by Masiello and co-workers[36] can be used to study plasmon excitations in large systems with arbitrary geometries. At the same time, it is not trivial to extend *e*-DDA method to time-domain modeling, as in the current work. Our simulation gives a novel perspective on the electron- and energy-transfer dynamics, focusing on the geometric structure of the nanoparticle−TiO_2 system, its

dx.doi.org/10.1021/ja5001592 | J. Am. Chem. Soc. 2014, 136, 4343−4354

electronic properties, the nuclear dynamics and electron−vibrational coupling, the mechanisms responsible for the electron injection, the electron−phonon relaxation process, and the electron−hole recombination. The results show excellent agreement with the available experimental data. Perhaps most importantly, the simulation demonstrates that charge separation occurs simultaneously with the photoexcitation of the plasmon band in 50% of the cases. The traditional ET mechanism, Figure 1b, operates in the remaining 50% of the time and is faster than the electron−phonon relaxation.

2. THEORETICAL METHODOLOGIES

The nonadiabatic MD simulation of ET dynamics is carried out using the mixed quantum-classical approach,[37] implementing the fewest switches surface hopping (FSSH) technique[38−40] within TDDFT[41−43] in the KS representation.[44] The electrons are treated quantum mechanically, and the nuclei are treated semiclassically, since they are much heavier and slower. The decoherence correction[34] to FSSH is used to study the electron−hole recombination. The following subsections outline the TDDFT-nonadiabatic MD and FSSH methods and provide the technical details of the standard DFT and MD techniques,[45] underlying the more advanced methodologies.

2.1. Time-Dependent KS Theory for Electron−Nuclear Dynamics. The ET dynamics including the nonadiabatic effects[46] are described by real-time TDDFT within the KS approach.[17,40] The electron density, $\rho(\mathbf{r},t)$, is expressed by the sum of the densities of the occupied time-dependent single-electron KS orbitals, $\varphi_p(\mathbf{r},t)$.

$$\rho(\mathbf{r}, t) = \sum_{p=1}^{N_e} |\varphi_p(\mathbf{r}, t)|^2 \tag{1}$$

The evolution of the electron density is determined by the time-dependent variational principle, leading to a set of single-particle equations for the evolution of the KS orbitals:

$$i\hbar\frac{\partial\varphi_p(\mathbf{r}, t)}{\partial t} = H(\mathbf{r}, \mathbf{R}, t)\varphi_p(\mathbf{r}, t); \quad p = 1, 2, \ldots, N_e \tag{2}$$

The equations are coupled, because the DFT Hamiltonian H depends on the overall electron density. The electron−vibrational interaction enters the Hamiltonian H through the external potential created by the nuclei. The time-dependent single-electron orbitals in eq 2 are expressed in the basis of the adiabatic KS orbitals, $\tilde{\varphi}_p(\mathbf{r},\mathbf{R}(t))$, which are calculated for the current atomic positions $\mathbf{R}$. The focus is on the evolution of the orbital φ_{PE} occupied by the photoexcited electron. As discussed previously,[47−50] the ET dynamics are well described by the evolution of the photoexcited electron, which involves unoccupied orbitals of the gold cluster and TiO_2 conduction band states. The populations of the other orbitals do not change over the course of the simulation: The hole resides near the Fermi energy, in particular, the Au_{20} highest occupied molecular orbital (HOMO), while the rest of the Au_{20} valence band orbitals and all TiO_2 valence band orbitals are occupied.

The adiabatic representation of the time-dependent KS orbital occupied by the photoexcited electron is given in eq 3:

$$\varphi_{PE}(\mathbf{r}, t) = \sum_k c_k(t)\tilde{\varphi}_k(\mathbf{r}; \mathbf{R}(t)) \tag{3}$$

Inserting eq 3 into eq 2 leads to the equation describing the evolution of the expansion coefficients:

$$i\hbar\frac{\partial}{\partial t}c_j(t) = \sum_k c_k(t)(\varepsilon_k\delta_{jk} + d_{jk}) \tag{4}$$

where ε_k is the energy of the adiabatic state k, and d_{jk} is the nonadiabatic coupling between states k and j. The nonadiabatic coupling is created by motion of atoms and represents the electron−vibrational interaction. It is calculated numerically as the overlap of orbitals j and k at sequential time steps:

$$\begin{aligned} d_{jk} &= -i\hbar\langle\tilde{\varphi}_j|\nabla_{\mathbf{R}}|\tilde{\varphi}_k\rangle\cdot\frac{d\mathbf{R}}{dt} = -i\hbar\langle\tilde{\varphi}_j|\frac{\partial}{\partial t}|\tilde{\varphi}_k\rangle \\ &\approx -\frac{i\hbar}{2\Delta t}(\langle\tilde{\varphi}_j(t)|\tilde{\varphi}_k(t+\Delta t)\rangle - \langle\tilde{\varphi}_j(t+\Delta t)|\tilde{\varphi}_k(t)\rangle) \end{aligned} \tag{5}$$

2.2. ET Mechanisms. The extent of ET from the gold nanoparticle to the TiO_2 surface is computed by integrating the photoexcited electron density over the region of the simulation cell occupied by the Au_{20} QD, Figure 2:

$$\begin{aligned} \int_{QD}\rho_{PE}(\mathbf{r}, t)d\mathbf{r} &= \int_{QD}|\varphi_{PE}(\mathbf{r}, t)|^2 d\mathbf{r} \\ &= \sum_{k,j} c_k^*(t)c_j(t)\int_{QD}\tilde{\varphi}_k^*(\mathbf{r}, \mathbf{R}(t))\tilde{\varphi}_j(\mathbf{r}, \mathbf{R}(t))d\mathbf{r} \end{aligned} \tag{6}$$

The time-derivative of eq 6 gives expressions for the adiabatic and nonadiabatic ET contributions:

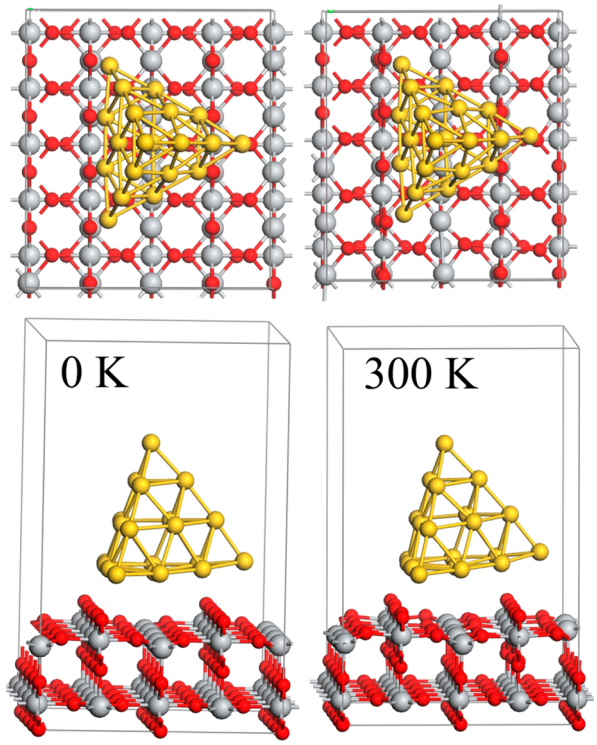

Figure 2. Top and side views of the simulation cell showing the geometry of the rutile $TiO_2(110)$-Au_{20} system optimized at 0 K (left) and during the molecular dynamics run at 300 K (right). No chemical bonding between the subsystems is seen, and only minor thermal fluctuations in the system geometry are observed at ambient temperature.

dx.doi.org/10.1021/ja5001592 | J. Am. Chem. Soc. 2014, 136, 4343−4354

$$\frac{d\int_{QD}\rho_{PE}(\mathbf{r},t)\mathrm{d}\mathbf{r}}{\mathrm{d}t} = \sum_{k,j}\left\{\frac{d(c_i^*c_j)}{\mathrm{d}t}\int_{QD}\phi_i^*\phi_j\mathrm{d}\mathbf{r} + c_i^*c_j\frac{d\int_{QD}\phi_i^*\phi_j\mathrm{d}\mathbf{r}}{\mathrm{d}t}\right\} \quad (7)$$

The first term has fixed localizations of adiabatic states, $\int_{QD}\phi_i^*\phi_j\mathrm{d}\mathbf{r}$, but changing expansion coefficients, $c_i^*c_j$, defining state occupations. The second term has fixed adiabatic state occupations but changing localizations. The first and second terms correspond to nonadiabatic ET and adiabatic ET, respectively. The adiabatic ET proceeds by a change in the localization of the photoexcited state from the gold QD to the TiO_2 surface, induced by atomic motions. To undergo a nonadiabatic transfer, the photoexcited electron has to hop into a TiO_2 state, causing a change in the state occupations.

The ET mechanisms carry different implications for the variation of the interface conductance and solar cell voltage with system properties. Direct ET usually requires strong donor−acceptor coupling, and the photoexcited state is shared by donor and acceptor materials. Direct electron injection implies that positive and negative charges are created at the energy of the absorbed photon. This fact can be used to avoid energy and voltage losses to heat. Adiabatic ET also requires strong donor−acceptor interaction as well as an energy fluctuation that can drive the system along the reaction coordinate and across the transition state. Adiabatic electron injection can take place near the edge of TiO_2 conduction band, potentially avoiding energy losses to heat.[50] Nonadiabatic ET does not require strong donor−acceptor interaction and, therefore, occurs in a broader range of systems. Nonadiabatic ET can be ultrafast in the presence of a high density of acceptor states. As the distance between the donor and acceptor species increases and the donor−acceptor coupling decreases, adiabatic ET becomes insignificant, and ET proceeds by the nonadiabatic mechanism, showing exponential dependence on the distance. The adiabatic and nonadiabatic mechanisms represent opposite limits are described by different analytic formulas and exhibit dissimilar dependence of the ET rate on system properties. Therefore, establishing the ET mechanism is of both fundamental and practical importance. A more detailed discussion of the ET mechanisms can be found in our recent work on the graphene−TiO_2 system[51] and a number of reviews.[52−54]

2.3. Fewest Switches Surface Hopping. The dependence of the electronic Hamiltonian on nuclear coordinates, eq 2, determines the influence of vibrational motions on the electronic evolution. The opposite effect, the back-reaction of electrons onto the nuclei, constitutes an essential part of a nonadiabatic MD algorithm. FSSH provides a prescription for the back-reaction, both allowing for branching between alternative reaction pathways[38] and satisfying detailed balance between transitions upward and downward in energy.[44] The latter is required for proper treatment of electron−vibrational energy exchange.[55]

The probability of a transition from an initial state k to another state j within the time interval δt is given in FSSH by[38]

$$g_{jk}(t,\delta t) = \max\left(0, \frac{b_{jk}\delta t}{a_{kj}(t)}\right) \quad (8)$$

where

$$a_{kj} = c_k(t)c_j(t)$$

and

$$b_{kj} = 2\hbar^{-1}\mathrm{Im}(a_{kj}\langle\tilde{\varphi}_k|H|\tilde{\varphi}_j\rangle) - 2\mathrm{Re}(a_{kj}\mathbf{d}_{kj}) \quad (9)$$

If the calculated g_{jk} is negative, the hopping probability is set to zero; a hop from state j to state k can take place only when the electronic occupation of state j decreases and the occupation of state k increases. To conserve the total electron−nuclear energy after a hop, the original FSSH technique rescales the nuclear velocities along the direction of the nonadiabatic coupling. If a nonadiabatic transition to a higher energy electronic state is predicted by eq 8 and the kinetic energy available in the nuclear coordinates along the direction of the nonadiabatic coupling is insufficient to accommodate the increase in the electronic energy, then the hop is rejected. The velocity rescaling and hop rejection give the detailed balance between the upward and downward transitions in energy.[44] The current simulation uses a simplified version of FSSH, as described in ref 56. If the energy exchanged between the electronic and nuclear degrees of freedom during a hop is rapidly exchanged among all nuclear modes, the energy distribution is Boltzmann at all times. Then, the velocity rescaling and hop rejection can be replaced by multiplying the probability, eq 8, for transitions upward in energy by the Boltzmann factor.

2.4. Decoherence Correction in Surface Hopping. The original FSSH[38] does not involve decoherence that takes place in the electronic subsystem due to coupling to quantum vibrations.[34,57,58] Decoherence can be ignored if it is slower than the time of quantum transitions.[37,50] This condition is satisfied for ET from the Au_{20} nanocluster to the TiO_2 surface, since it involves multiple rapid hops between closely spaced electronic states. In contrast, the return of the injected electron to the gold QD involves an electronic transition across a wide energy gap. It takes place on picosecond time scale,[11] which is significantly longer than the decoherence time. Therefore, a semiclassical decoherence correction should be included with SH.[46,55,57,58] In the current simulation, the time-dependent KS wave function $\varphi_{PE}(\mathbf{r},t)$ is collapsed to an adiabatic eigenstate $\tilde{\varphi}_k(\mathbf{r};\mathbf{R}(t))$, eq 3, on the decoherence time scale, as implemented in ref 34. The collapse procedure is equivalent to resetting to zero the off-diagonal matrix elements a_{kj}, eq 9, entering the FSSH transition rate, eq 8. The collapse times are determined by a sequence of random numbers sampled from the Poisson distribution with the characteristic time determined by the decoherence time. The probability of collapse onto eigenstate k is given by the square of the coefficient $c_k(t)$ at the collapse time. The decoherence time was computed as the pure-dephasing time in the optical response formalism, according to the following procedure. The fluctuations ΔE in the electronic excitation energy E caused by atomic motions are characterized by the energy autocorrelation function

$$C(t) = \langle\Delta E(t)\Delta E(0)\rangle_T \quad (10)$$

The brackets indicate averaging over a canonical ensemble. The autocorrelation function is usually normalized

$$C_{\mathrm{norm}}(t) = \frac{\langle\Delta E(t)E\Delta(0)\rangle_T}{\langle\Delta E^2(0)\rangle_T} \quad (11)$$

by its initial value $C(0) = \langle\Delta E^2(0)\rangle_T$. The square root of this value gives the average fluctuation of the excitation energy.

dx.doi.org/10.1021/ja5001592 | J. Am. Chem. Soc. 2014, 136, 4343−4354

The pure-dephasing function is computed using the second-order cumulant expansion to the optical response function, as described, for example, in ref 59:

$$D_{\mathrm{cumu}}(t) = \exp(-g(t)) \tag{12}$$

where $g(t)$

$$g(t) = \int_0^t \mathrm{d}\tau_1 \int_0^{\tau_1} \mathrm{d}\tau_2 C(\tau_2) \tag{13}$$

Typically for condensed phase systems, the cumulant representation of the pure-dephasing function converges rapidly and gives an accurate description.[60,61] Fast convergence is important for *ab initio* simulations, which are limited to picoseconds. Fitting eq 12 by a suitable analytic function, typically Gaussian, gives the pure-dephasing time.

2.5. Simulation Details. The simulation uses the stoichiometric rutile (110) surface, since it is most stable among the low index surfaces of rutile TiO_2.[62] The 120-atom (5×2) surface region was modeled with a periodically repeated slab, comprised of six atomic layers of TiO_2 with the bottom three layers frozen in the bulk configuration. The slab was separated from its periodic image along the surface normal by a large, 20 Å vacuum region. The tetrahedral Au_{20} cluster, chosen due to its high symmetry (T_d) and stability, represented the gold QD.[63,64] The cluster geometry corresponds to fcc bulk gold, with the cluster surfaces forming the (111) planes. The Au_{20} cluster preserves the semiconductor bulk structure during both geometry optimization and finite-temperature MD simulation. Initially, the gold atoms in the bottom plane of Au_{20} connect to six bridging oxygen atoms of the TiO_2 (110) surface. This setup maximizes the number of direct Au_{20}–TiO_2 interactions and creates the most stable configuration.

The geometry optimization, electronic structure, and adiabatic MD calculations are performed using the projector augment wave method implemented in the Vienna *ab initio* simulation package (VASP).[65] The electron exchange and correlation terms are treated with the Perdew–Burke–Ernzerhof (PBE) functional.[66] The DFT+U[67] approach is used to describe the TiO_2 properties. The on-site U = 6.0 eV and J = 0.5 eV values are applied to treat the 3d electrons of Ti atoms.[68] After relaxing the geometry at 0 K, repeated velocity rescaling is used to bring the temperature of the Au_{20}–TiO_2 system to 300 K, corresponding to the temperature in the experiment.[11] After that, a 3 ps adiabatic MD simulation is performed in the microcanonical ensemble with a 1 fs atomic time-step.

To simulate the photoinduced ET dynamics, 100 initial system geometries are selected randomly from the 3 ps adiabatic MD trajectory. An electron is promoted to the orbital corresponding to the lowest energy plasmonic excitation of Au_{20}, and its evolution is tracked by solving eq 4, using the second-order differencing scheme and a 10^{-3} fs electronic time-step. This procedure is applied to study the competing ET and energy relaxation processes within the manifold of Au_{20} and TiO_2 conduction band states. The electronic energy is computed as the standard quantum mechanical expectation value, averaged canonically over multiple nonadiabatic MD runs. The electron–hole recombination is simulated with the decoherence-corrected nonadiabatic MD-FSSH scheme, outlined in the previous subsection. Since the ET and electron–phonon energy relaxation occur much faster than the electron–hole recombination, it is assumed that the electron had relaxed to the lowest energy unoccupied molecular orbital (LUMO) prior to the recombination. The recombination process is modeled within the two-state HOMO–LUMO approximation, requiring evaluation of only one pure-dephasing time scale. This time scale determines the homogeneous luminescence line-width and can be tested experimentally, as done previously for a variety of systems.[69−73]

3. RESULTS AND DISCUSSION

The time-domain *ab initio* simulations of the plasmon-driven electron injection and recombination in the Au_{20}–TiO_2 system provide a detailed real-time atomistic picture of the electron and energy transfer, energy relaxation, and electron–hole recombination dynamics at the interface. The nonadiabatic MD simulation allows us to explore and identify directly the ET mechanisms, the time scales of various competing processes, the elastic and inelastic electron–vibrational interactions, and the phonon modes that couple to the electronic subsystem. The simulation results can be compared directly with the corresponding time-resolved experiments. The simulation establishes that the direct photoexcitation mechanism generates a large contribution to the photoinduced charge separation in the plasmonic system. The discussion in the following subsections emphasizes a number of issues related to the electron–vibrational dynamics, including the geometric and electronic structure of the interface, vibrational dynamics, plasmon-driven ET from the gold nanoparticle into the TiO_2 conduction band, electron–vibrational energy relaxation, and electron–hole recombination.

3.1. Geometric Structure of the Au_{20}–TiO_2 System. The interaction between the Au_{20} nanocluster and the TiO_2 surface determines the rates and mechanisms of the electron- and energy-transfer processes.[74−76] The Au_{20}–TiO_2 geometry and separation characterize the strength of the interfacial interaction. The simulation uses the most common (110) surface of rutile TiO_2 and a medium size gold nanoparticle that is thermodynamically stable and preserves the topology of bulk gold. Figure 2 shows the top and side views of the systems relaxed at 0 K (left panel) and a geometry from the MD run at 300 K (right panel). The Au_{20} nanoparticle remains bound to the TiO_2 substrate at room temperature, even though thermal fluctuations affect the combined system geometry. In either case, the Au_{20} particle remains relatively close to the TiO_2 surface, although no directional, covalent-type bonds are formed between the subsystems. This behavior differs from all previously studies cases, including the molecule–semiconductor interfaces,[49,52,77−80] the wet-electron system,[48] the PbSe QD–TiO_2 interface,[47] and the graphene–TiO_2 composite.[51] While the molecules sensitizing TiO_2 are designed to bind covalently, neither the PbSe QD nor graphene systems include bridging chemical groups. Nevertheless, the Pb atoms formed strong bonds with the bridging oxygens of the rutile TiO_2 (110) surface,[47] and some of the graphene six-membered rings rearranged, freeing p_z electrons from the π-conjugated network and allowing them to interact with the TiO_2 oxygens.

The largest scale motion at ambient temperature is associated with in-plane oxygen atom displacements in the first layer of the TiO_2 surface and nanocluster movement perpendicular to the TiO_2 (110) surface. The displacements of the bridging oxygen atoms can be seen in the top views of the simulation cell, Figure 2. The movement of the nanocluster is demonstrated by the side views. The nanocluster becomes slightly more spherical at the elevated temperature. The average separation between Au_{20} and the surface increases from 2.125

dx.doi.org/10.1021/ja5001592 | J. Am. Chem. Soc. 2014, 136, 4343−4354

to 2.431 Å as temperature is raised from 0 to 300K. The increasing Au_{20}–TiO_2 separation serves to decrease the donor–acceptor coupling strength. This decrease can have a notable effect on the ET mechanism and may be partially responsible for nonadiabatic ET being the dominant mechanism, as shown below. Adiabatic ET requires a strong donor–acceptor interaction, while nonadiabatic ET operates in cases with a weaker interaction. Nonadiabatic ET is similar to tunneling and shows exponential dependence on the donor–acceptor separation.

3.2. Electronic Structure of the Au_{20}–TiO_2 Interface. Figure 3a shows the density of states (DOS) of the combined system, separated into the contribution from Au_{20} (black line) and the TiO_2 (110) slab (red line). The DOS of the isolated Au_{20} cluster and TiO_2 surface are shown in Figure S1. Since most pure DFT functionals, such as PBE used here, underestimate band gaps due to the self-interaction error,[66] the band gap of the current system was scaled to the experimental value of 1.1 eV.[11] The DOS demonstrates that the plasmon excitation band of the metallic nanocluster is well inside the TiO_2 conduction band. The high density of TiO_2 acceptor states available at the plasmon excitation energy facilitates efficient ET and favors the nonadiabatic ET mechanism. The Au_{20} DOS is low at energies from 1 to 2 eV above the Fermi energy and rises rapidly at 2.25 eV, coinciding with the onset of the plasmon band.[11] Comparing the combined DOS given in Figure 3a with the DOS of the individual subsystems shown Figure S1, we observe that the combined DOS resembles the sum of the DOS of the isolated subsystems. The peaks of the individual DOS are broadened by the interaction, and some small new features appear. The key bands present in the isolated subsystem DOS are also present in the combined DOS. The Fermi energy of TiO_2 is lower by about 2 eV relative to the Fermi energy of Au_{20}.

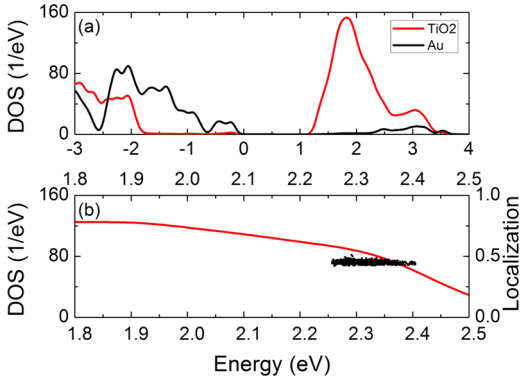

Figure 3. (a) DOS of the TiO_2(110) surface (red line) and Au_{20} nanocluster (black line). The Fermi level is set to zero. (b) TiO_2 DOS in the excitation energy range (red line) and localization of the plasmon excitation on the Au_{20} cluster (black squares). About 50% of the plasmon density extends onto TiO_2.

The DOS of the Au_{20}–TiO_2 (110) system, Figure 3a, gives rise to the absorption spectrum, shown in Figure S2. The strongest peak at 2.3 eV corresponds to the plasmon excitation of the Au_{20} particle. It is excitation of this peak that is sampled in the reported time-domain simulation, as illustrated by the black points in Figure 3b. The LUMO of the combined Au_{20}–TiO_2 system is due to TiO_2, while the HOMO arises from Au_{20}, Figure 3a. This setup indicates that the lowest electronically excited state of the system is a charge-transfer state. Indeed, the absorption spectrum, Figure S2, shows a lower intensity peak at 1.7 eV, corresponding to the charge-transfer excitation. The peaks in the spectrum at 2.7 eV and higher have contributions from both TiO_2 and Au_{20}.

Following the plasmon-initiated ET process, the system will evolve to the lowest excited state on a subpicosecond time scale as a result of phonon-induced relaxation of the electron to the conduction band edge. Further electron–phonon relaxation can lead to electron–hole recombination, which competes with electron delocalization into TiO_2 bulk and constitutes the primary source of losses in the photoinduced current and photocatalytic efficiency. These processes are accounted for in the time-domain simulation discussed below.

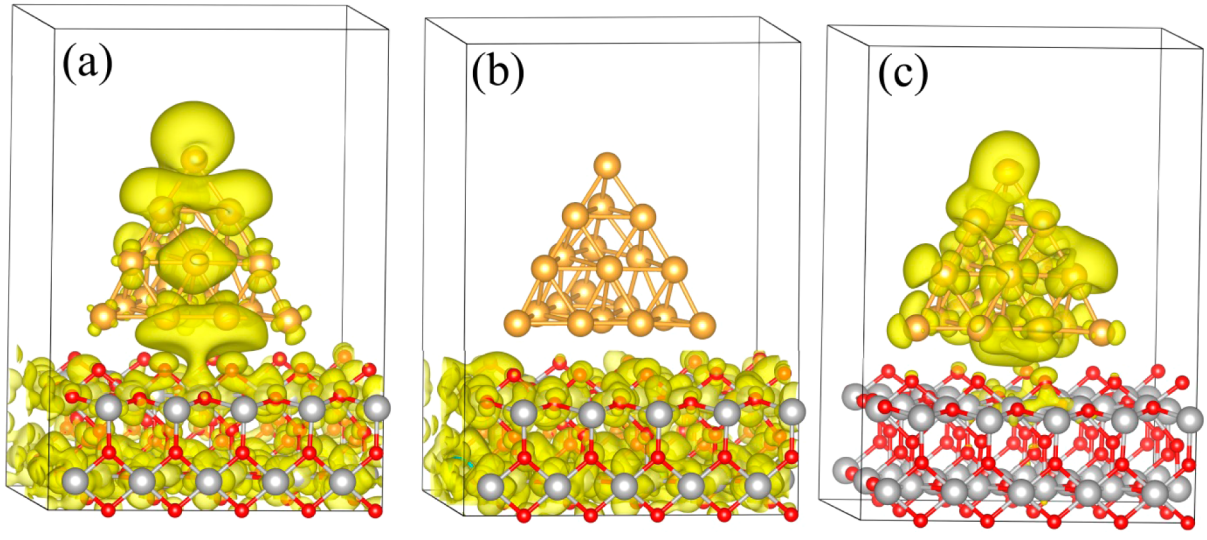

Figure 4. Charge densities of (a) plasmon, (b) TiO_2 acceptor state, and (c) HOMO of the Au_{20}–TiO_2 system. The excited surface plasmon, state (a), is delocalized significantly onto TiO_2, leading to instantaneous generation of the charge-separated state upon photoexcitation at the plasmon energy. Entropy drives the electron into TiO_2 bulk, exemplified by state (b). Following electron–vibrational relaxation, the electron can recombine with the hole, residing in state (c), on a picosecond time scale.

dx.doi.org/10.1021/ja5001592 | J. Am. Chem. Soc. 2014, 136, 4343–4354

In the continuous-wave excitation limit describing sunlight absorption, a system is excited to an adiabatic state, i.e., an eigenstate of the electronic Hamiltonian for fixed nuclear positions. If the donor and acceptor state energies are in near resonance and the donor−acceptor coupling is significant, the adiabatic state becomes a superposition of the donor and acceptor states. The coupling occurs due to interaction of the Au 5d orbitals with the 3d orbitals of the under-coordinated Ti atoms of the surface, facilitated by the surface oxygens. Figure 3b shows localization of the excited state on the Au_{20} donor (black dots), indicating that continuous-wave light generates a state that is already about 50% delocalized onto the TiO_2 acceptor. Figure 4 presents the spatial distribution of electron densities of the donor and acceptor states for electron injection process. The donor state is distributed about equally between the Au_{20} pyramid and the TiO_2 substrate, Figure 4a. This result indicates that in 50% of the cases, excitation of the plasmon band instantaneously generates the charge-separated state. This characteristic is different from a typical plasmon,[31,81−83] with the majority of the density localized on the nanoparticle surface and in regions of high curvature, on top of the Au_{20} pyramid. The acceptor state is spread nearly uniformly across the TiO_2 slab, Figure 4b. This is in contrast, for instance, with chromophore-sensitized TiO_2, in which case directional chromophore−TiO_2 covalent bonding creates a localized acceptor state.[80]

3.3. Nuclear Dynamics. Nuclear motions modulate both energy and localization of the excited state. Fluctuations in the atomic positions generate an ensemble of inhomogeneous initial conditions prior to the photoexcitation. Further, nuclear motions drive the system across a transition state during adiabatic ET and generate the nonadiabatic coupling. On one hand, atomic motions shift the adiabatic state densities between the donor and acceptor species, changing state localizations and inducing adiabatic ET. On the other hand, they cause transitions between adiabatic states: the nonadiabatic coupling is directly proportional to the nuclear velocity, $d\boldsymbol{R}/dt$, eq 5.

The dots in Figure 3b show the localization of the photoexcited state on the gold cluster for different times along the MD trajectory. The localization changes vary little along the MD trajectory. This fact agrees with the fundamental properties of surface plasmons, which are located away from the nanoparticle and are largely decoupled from phonons. In comparison, the photoexcited states of other systems sensitizing TiO_2 are significantly more sensitive to vibrational motions.[47,48,51,80]

The Fourier transforms of the time-dependent photoexcited-state energy and localization identify the phonon modes that are coupled to the electronic subsystem. The Fourier transforms are shown in Figure 5, together with the normalized autocorrelation functions of the state energy and localization. The nonadiabatic electron−phonon coupling is directly related to the second derivative of the energy along the nuclear trajectory.[84] Therefore, the vibrational modes that most strongly modulate the energy levels create the largest coupling.[37,85] The autocorrelation function describes how the energy at a particular time depends on its value at earlier times. Poorly correlated, random motions result in autocorrelation functions that decrease rapidly from 1 to 0. Well-correlated, periodic motions lead to autocorrelation functions that oscillate between 1 and −1.

The Fourier transforms show that low-frequency vibrational modes couple to the electronic excitation more strongly than

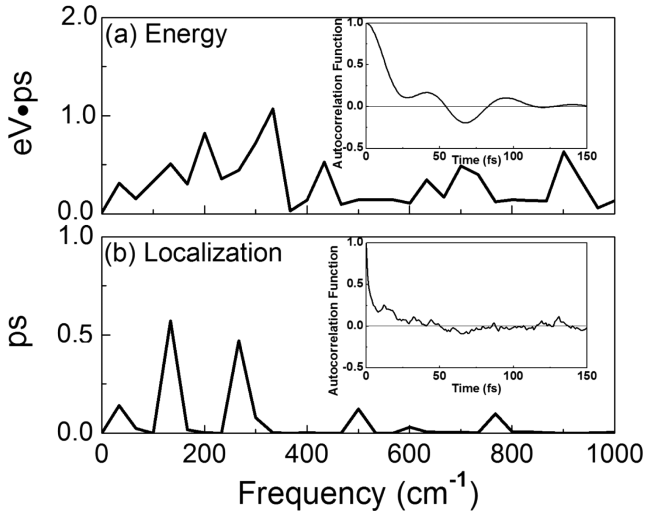

Figure 5. Fourier transforms of the phonon-induced fluctuation of the photoexcited plasmon (a) energy and (b) localization. The inserts show the autocorrelation functions of the plasmon energy and localization.

high-frequency modes, Figure 5. This is in agreement with the previous studies.[85,86] Phonon modes with frequencies <400 cm^{-1} dominate both Fourier transforms. The localization Fourier transform has largest amplitude in the region between 100 and 300 cm^{-1}. Notable contributions from vibrations around 800 cm^{-1} are seen in both spectra. In particular, the mode at 700 cm^{-1} is responsible for the persistent oscillation of the energy autocorrelation function, Figure 5a. Since the plasmon excitation is delocalized onto the nanoparticle surface and the TiO_2 substrate, Figure 4a, its wave function is sensitive primarily to low-frequency acoustic phonons that modulate the size and shape of the nanoparticle. High-frequency optical modes involve local displacements of atoms, having little effect on the plasmon excitation.[85,86] They couple to the photoexcited state primarily due to the state delocalization onto the TiO_2 substrate. High-frequency TiO_2 vibrations change dipole moments of the polar Ti−O bonds, and therefore, they couple to the electronic subsystem.

The peaks in the calculated Fourier transforms can be assigned to the following vibrations. The peak around 50 cm^{-1} is seen in both spectra shown in Figure 5. It is particularly strong in the energy Fourier transform and can be attributed to the low-frequency 1E mode of Au_{20}.[87] The energy Fourier transform also shows several moderate peaks at middle and high frequencies, arising from a series of transverse acoustic (TA), transverse optical (TO), and longitudinal optical (LO) modes. For example, the peak at 250 cm^{-1} corresponds to the coupled LO modes of rutile.[88] The higher frequency signals are overtone combinations of the lower frequency phonons. The TiO_2 modes contribute to the calculated Fourier transform spectra, since the photoexcited state delocalizes onto the TiO_2 slab.

The modes seen in the Fourier transform spectrum for the photoexcited state localization are somewhat different from the phonons that modulate the state energy. The localization is more sensitive to changes in the wave function than the energy, since the energy is computed by averaging over the whole wave function. The localization Fourier transform shows a strong peak around 135 cm^{-1}, a slightly weaker peak at 270 cm^{-1}, and a few weak signals in the range between 400 and 800 cm^{-1}. The

dx.doi.org/10.1021/ja5001592 | J. Am. Chem. Soc. 2014, 136, 4343−4354

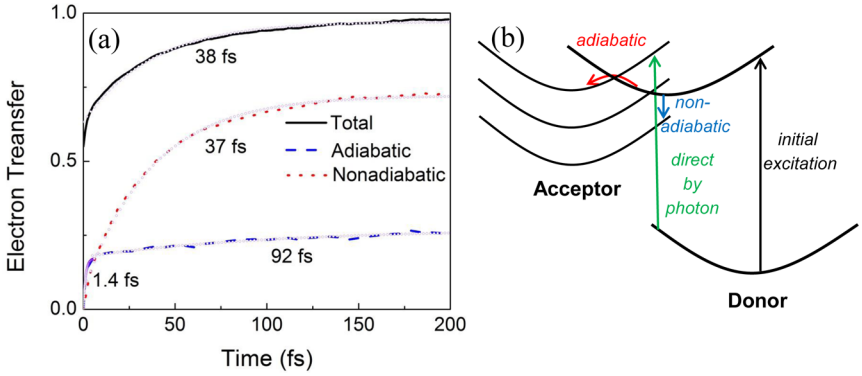

Figure 6. (**a**) Average ET dynamics. The solid black, dashed blue, and dotted red lines represent the total, adiabatic, and nonadiabatic ET, respectively. The open circles are fits (eq 14) with the time-scales (τ) shown in the figure. Nonadiabatic ET provides the dominant ET mechanism due to relatively weak donor–acceptor coupling and high density of states. (**b**) Schematic of the photoinduced ET mechanisms. The photoexcited donor can transfer the electron to the acceptor adiabatically by passing over a transition state barrier (curved red arrow). Alternatively, the transfer can occur nonadiabatically, via a hop between donor and acceptor states away from the transition state (downward blue arrow). Photoexcitation can promote the electron directly from the donor to the acceptor (upward green arrow).

135 cm^{-1} peak corresponds to the triply generate vibration (t_2) in bare Au_{20} with T_d symmetry.[64] In a perfectly symmetric cluster, the vibration is at 148 cm^{-1}.[64] Here, minor dilation and distortion of the Au_{20} cluster, arising due to heating and interaction with TiO_2, lead to a small blue-shift. The peak at 270 cm^{-1} is the double overtone of the main vibration at 135 cm^{-1}. This mode is also close to the coupled LO modes of TiO_2 at 255 cm^{-1}.[88]

Thermal fluctuations of atomic coordinates create an inhomogeneous ensemble of initial conditions for the plasmon-driven dynamics. The black dots in Figure 3b represent the distribution of the photoexcited state energy. Its width is several tenths of eV, on the order of the plasmon resonance line-width.[11] The distribution starts at 2.25 eV, coinciding with the onset of the plasmon band.[11] Figure 3b also presents the TiO_2 DOS within the energy region containing the photoexcited state. The TiO_2 DOS varies slowly, indicating that states in the plasmon band interact, on average, with the same number of TiO_2 surface states, rationalizing why the donor–acceptor state mixing and the photoexcited state localization are virtually independent of energy.

The autocorrelation functions of the photoexcited state energy and localization, insets in Figure 5, decay quite rapidly; nevertheless, there are substantial differences between the two functions. The initial decay in the energy autocorrelation function occurs within 25 fs. The initial decay of the localization autocorrelation function requires only 10 fs. On the longer time scale, the energy autocorrelation function continues to oscillate with a 50 fs period for several periods, while the localization autocorrelation function shows only one minor recurrence. The comparison indicates that the electronic donor–acceptor coupling, determining the extent of the photoexcited state delocalization between the gold nanoparticle and the TiO_2 surface, is more sensitive to the positions of the nuclei than the state energy.

3.4. Electron Transfer Dynamics. The delocalization of the photoexcited state between Au_{20} and TiO_2 indicates that the charge-separated state is created upon excitation of the Au_{20} plasmon band with a 50% probability. The remaining 50% of the cases involve a distinct ET step. The simulated ET occurs on a 40 fs time scale, Figure 6a, in agreement with the experimentally determined 240 fs upper bound.[11] The gold nanocluster used in the simulation is smaller than those employed in experiments, and therefore, one can expect more significant overlap and stronger coupling between the donor and acceptor states, leading to faster ET.

Both the contribution of direct ET by photoexcitation and the time needed to transfer remaining fraction of the photoexcited electron from Au_{20} cluster to TiO_2 depend on the donor–acceptor interaction. The ET coordinate is defined by integrating the photoexcited electron density over the region of the simulation cell occupied by the electron acceptor, that is, TiO_2, eq 6. The initial ET coordinate shown in the y-axis of Figure 6a gives the contribution of the direct ET mechanism, Figure 6b, to the overall ET process. The time scales and relative amounts of adiabatic and nonadiabatic electron injection are calculated by separating the overall evolution of the ET coordinate into the contributions due to changes in the localization and occupation, respectively, according to eq 7. Figure 6a demonstrates that nonadiabatic ET is the dominant mechanism, responsible for about 75% of the ET amplitude. The adiabatic mechanism contributes around 25%. Adiabatic ET relies on strong electron–phonon coupling, while non-adiabatic ET can operate with weaker coupling and is accelerated by a high density of acceptor states. The coupling is relatively weak in the present system, since no chemical bonds exist between the gold nanoparticle and the TiO_2 substrate. At the same time, the DOS of the TiO_2 acceptor is high. These two factors rationalize the nonadiabatic mechanism. The situation is similar to that in the graphene–TiO_2 system.[51]

The time scales, τ, of the total, adiabatic and nonadiabatic ET were obtained by fitting the data with the exponential function

$$f(t) = f_0 + A\exp(-t/\tau) \quad (14)$$

The time scales are reported in Figure 7a. The time of ET from the Au_{20} particle to the TiO_2 surface is longer than the time required for a collective surface plasmon excitation to separate into electron–hole pairs. The latter process occurs on a 10 fs time scale.[89] Thus, the sequence of events leading to the plasmon-driven charge separation at the interface between a gold nanocluster and a TiO_2 surface starts by excitation of a gold surface plasmon exhibiting notable delocalization onto the TiO_2 surface. In 50% of the cases, the plasmon separates into electron–hole pairs on a 10 fs time scale, and on a 40 fs time scale the electron transfers into TiO_2. These processes are

dx.doi.org/10.1021/ja5001592 | J. Am. Chem. Soc. 2014, 136, 4343–4354

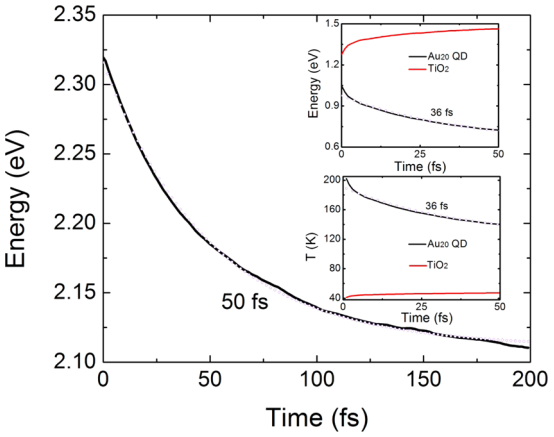

Figure 7. Decay of the electronic excitation energy of the TiO_2–Au_{20} system, caused by coupling to phonons. The insert shows the transient heating of TiO_2 due to energy losses by Au_{20} driven by ET from Au_{20} to TiO_2.

accompanied by electronic energy loss to heat due to coupling to phonons, as discussed in the next section.

The conclusions drawn about the plasmon-induced ET dynamics on the basis of the above calculations may be affected by a number of factors, including approximations made during the calculations and the experimental conditions. To test the former, we employed a more advanced DFT functional. To test the latter, we incorporated defects within both subsystems. Using the range-separated hybrid functional HSE06,[90] we optimized the geometry of the Au–TiO_2 system and carried out a short MD trajectory. Figure S3 shows the excited plasmon densities obtained with the HSE06 functional at 0 K and at ambient temperature. Similarly to Figure 4a, the densities extend from the gold nanoparticles onto the TiO_2 surface, supporting the conclusion that there exists a significant probability of ET immediately during photoexcitation of a plasmonic particle.

Realistic systems often contain defects. To mimic this situation, we created defects in each subsystem. We removed a bridging oxygen atom from the TiO_2 surface to create an oxygen vacancy. Separately, we removed a gold atom from a corner of Au_{20} to create a defect in the nanoparticle. Then, we optimized the structure of the two systems with defects, and calculated the electronic structure with the hybrid HSE06 functional.[90] The removed atoms are indicated in part a of Figure S4, while the plasmon densities are shown in parts b and c. The unsaturated chemical bonds arising due to the missing atoms increase the donor–acceptor interaction, leading to further delocalization of the plasmon excitation onto TiO_2. Thus, defects create favorable conditions for ET from the nanoparticle to the substrate already during excitation of the plasmon band. Defects should also accelerate ET if it occurs subsequent to the photoexcitation.[91]

3.5. Energy Relaxation. Electron–phonon relaxation parallels the ET process and results in electronic energy loss to heat. In gold and other metals, all electronic energy is rapidly deposited into vibrations, and photogenerated electrons and holes quickly recombine, in the absence of a bias voltage. Semiconductors, such as TiO_2, have a gap between the conduction and valence bands. As a result, electrons and holes decay to the edges of the corresponding bands and survive for long times. The metallic Au_{20} cluster is sufficiently small to exhibit a band gap due to quantum confinement. Therefore, the electron–hole recombination requires time. Since the bottom of the conduction band in the Au_{20}–TiO_2 system is formed by Au_{20}, while TiO_2 creates the top of the valence band, Figure 3a, the electron–phonon relaxation results in a charge-separated state.

Figure 7 characterizes the electron–vibrational energy relaxation. The simulation data are fitted by eq 14. The 50 fs electronic energy relaxation is somewhat slower than the 40 fs ET, Figure 6a. In systems involving larger Au clusters, the relaxation can be faster than the ET, because larger cluster have more states, and higher density of states generally speeds up electron–phonon energy exchange. However, the similarity in the ET and energy relaxation times does not present a problem in the current system, because it maintains a large band gap, Figure 3a. This situation is in contrast to the graphene–TiO_2 system, since graphene is a metal. Efficient charge separation in this case requires ET to be faster than relaxation.[11] The insert in Figure 7 separates the total excess energy into contributions stemming from Au_{20} and TiO_2. Because ET is faster than the relaxation, the TiO_2 surface heats up transiently by about 40 K. Photon absorption by the Au_{20} particle increases its temperature by as much as 200K.

Following ET and simultaneously with the electron–phonon relaxation, the electron delocalizes from the TiO_2 surface into bulk. The Coulomb interaction between the electron and the hole acts to keep the electron near the interface; however, the density of bulk TiO_2 states accessible to the electron significantly exceeds the density of surface states, and the electron is driven into the bulk by entropy. Computational modeling of the delocalization process[52] requires large simulations cells. At the same time, a realistic system contains surface defects, such as oxygen vacancies.[92] The defects trap the electron at the surface, leading to a relatively rapid electron–hole recombination observed in the experiment.[11] The recombination process is studied in the following section.

3.6. Electron–Hole Recombination. The time scales characterizing the transfer of the injected electron back to the gold nanoparticle range from picoseconds to nanoseconds.[11] The fast components arise due to electron trapping at the interface, while the slower components involve electron diffusion within TiO_2 bulk, followed by return to the surface, generally in a location different from the injection site. One can expect that the times and amplitudes of the longer components should depend strongly on the TiO_2 substrate preparation, including such factors as the size and roughness of TiO_2 particles, their interconnectivity, amount of surface and bulk defects, etc. The fast component should be present in all samples, and its amplitude should be reduced in samples with few TiO_2 surface defects and good TiO_2 particle interconnectivity, favoring electron transport to the electrode or photocatalytic site. The current simulation cell, Figures 2 and 4, allows us to study the fast component of the electron–hole recombination, associated with electrons confined at the interface.

Participation of the phonon modes is key to the recombination: the initial and final states for this process are separated by a large energy gap, and the excess electronic energy is accommodated by phonons. It is very unlikely that a nuclear fluctuation can bring the initial and final electronic states in resonance, necessitating a nonadiabatic transition. Thus, the transfer of the electrons back to the Au_{20} cluster proceeds exclusively by the nonadiabatic mechanism.

dx.doi.org/10.1021/ja5001592 | J. Am. Chem. Soc. 2014, 136, 4343–4354

Figure 4b,c depicts the orbital densities of LUMO and HOMO, which constitute the initial and final states for the electron−hole recombination. The LUMO is spread nearly uniformly across the TiO_2 slab. The HOMO is localized on Au_{20} and extends into the TiO_2 substrate. The HOMO delocalization into TiO_2 is required to create the nonadiabatic coupling and to achieve the electron−hole recombination. Both elastic and inelastic electron−phonon scattering affects the recombination process. Inelastic scattering accommodates the energy lost by the electron as it makes a transition from the LUMO to the HOMO. Elastic interactions induce more subtle effects. In particular, they destroy coherence formed between HOMO and LUMO. The elastic electron−phonon interaction is known as pure dephasing in optical measurements.[93,94] It determines the line-width of single particle luminescence. Luminescence from LUMO to HOMO is unlikely in the present system, since HOMO and LUMO are localized on different parts of the system, Figure 4b,c, and the relevant transition dipole moment is small. Instead, the LUMO to HOMO transitions occurs nonradiatively.

Figure 8a presents the Fourier transform of the HOMO−LUMO energy gap. The gap autocorrelation function is shown as an inset. The autocorrelation function is similar to that for the electron injection, inset of Figure 5a. However, the spectrum shows a significantly stronger contribution from the midfrequency vibrations in the 300−500 cm^{-1} energy window. This is to be expected, since the Au_{20} state involved in the electron−hole recombination is an ordinary bulk state localized directly on Au atoms. In contrast, the Au_{20} state participating in the initial ET is a delocalized surface plasmon. As shown earlier,[85] bulk-like states couple to higher frequency phonons than plasmons. The signal seen in the mid-frequency range can also be assigned, to the 366 and 430 cm^{-1} phonons, which are detected in rutile TiO_2.[95] Since TiO_2 has higher frequency phonons compared to Au, due to the presence of light O atoms, and since higher frequency motions generate stronger nonadiabatic coupling, the vibrational modes of TiO_2 contribute strongly to the back-ET process.

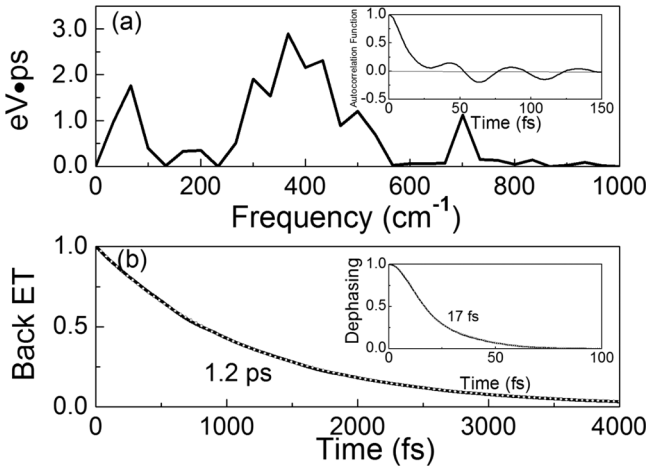

Figure 8. (a) Fourier transforms of the HOMO−LUMO energy gap, characterizing the nonadiabatic electron−phonon coupling responsible for electron−hole recombination. (b) ET from LUMO to HOMO, resulting in electron−hole recombination. The small circles show the fit by eq 15. The inserts of (a) and (b) display the autocorrelation function and pure-dephasing function, (eq 15), respectively, for the HOMO−LUMO energy gap.

The current simulation treats phonons classically, necessitating a semiclassical decoherence correction for the simulation of the electron−hole recombination.[34] The correction is needed here, because the elastic (pure-dephasing) time is significantly shorter than the quantum transition time. The situation is opposite for the initial ET process: multiple quantum transitions take place within the 40 fs time scale of the delocalized plasmon-driven ET. The pure-dephasing time for the electron−hole recombination is computed with the cumulant expansion, eqs 12 and 13. The resulting dephasing function is shown in inset of Figure 8b. It is fit with a combination of two Gaussians:

$$f(t) = B\exp(-0.5(t/\tau_a)^2) + (1 - B)\exp(-0.5(t/\tau_b)^2) \quad (15)$$

The obtained times are τ_a = 11 fs and τ_b = 27 fs. B gives the amplitude of the fast Gaussian. The pure-dephasing time is obtained by taking a weighted average of the two times:

$$T = B\tau_a + (1 - B)\tau_b \quad (16)$$

The 17 fs pure-dephasing time is significantly shorter than the 1 ps electron−hole recombination time reported in the experiment,[11] as should be expected for transitions across large energy gaps. The time-resolved electron−hole recombination signal is shown in Figure 8b. The calculated 1.2 ps time, obtained using the exponential fit, eq 14, agrees very well with the experimental data.[11] A similar back-ET time was found, for instance, in the alizarin−TiO_2 system.[52] The presented analysis shows that the 1 ps time scale reported in the experiments arises from recombination of the hole, remaining on the gold nanoparticle after the plasmon-driven ET, and the electron confined at the TiO_2 surface. In a realistic system, electrons are trapped near the surface by defect states. The current simulation includes no defects. One can expect that a defect state will accelerate the recombination, both because its energy will be somewhat below the TiO_2 conduction band edge and since localized states tend to create stronger electron−phonon nonadiabatic coupling.[34] Localized states exhibit higher frequency vibrations and hence larger nuclear velocity at a given temperature, eq 5. One can expect a larger value for the electronic overlap term as well, since the wave function of a surface trap should be closer to the nanoparticle than the wave function of a delocalized TiO_2 state.

4. CONCLUSIONS

In this paper, we reported a time-domain atomistic study of plasmon-driven ET, electron−phonon energy relaxation, and electron−hole recombination at the Au_{20}−TiO_2 interface. The simulations connect directly with the time-resolved experimental data. The obtained ET and electron−hole recombination time scales show excellent agreement with experiment. By performing atomistic simulations, we were able to provide a detailed analysis of the ET, relaxation and recombination processes, establish their mechanisms, characterize electronic states and phonon modes involved, and describe the interplay between the productive and unfavorable channels of photoinduced electron and energy flow.

We established that, with a 50% probability, the charge separation at the interface occurs immediately upon photoexcitation of the plasmon band. This novel mechanism of charge separation alters the traditional multistep description, in which the plasmonic excitation breaks into electron−hole pairs, and then electrons undergo charge transfer. Recent exper-

dx.doi.org/10.1021/ja5001592 | J. Am. Chem. Soc. 2014, 136, 4343−4354

imental studies of H-doped black titania[96] may provide another example of the instantaneous charge separation mechanism. There, the H-doped amorphous shell plays the same role as the metallic particles in the present system.

In the remaining 50% of the scenarios, the plasmon band excitation generates electron−hole pairs in the gold particle, and the electron is transferred to the TiO_2 surface on a sub-100 fs time scale. Electron−phonon energy relaxation parallels the electron injection and is somewhat slower. Driven by entropy due to the high density of bulk TiO_2 states, the electron overcomes the Coulombic electron−hole attraction and delocalizes into TiO_2 bulk. Structural defects in the TiO_2 surface can trap the injected electron near the gold nanoparticle, leading to a 1 ps electron−hole recombination. Electrons that have been able to diffuse into bulk TiO_2 can find their way back to the surface and recombine with the hole on a much longer time scale. The electron injection occurs primarily by the nonadiabatic mechanism, due to a relatively weak donor−acceptor coupling and a high density of TiO_2 acceptor states. The recombination proceeds exclusively by the nonadiabatic mechanism, because of the large energy gap between the initial and final states in this case.

The interaction between Au_{20} and the bare rutile TiO_2 (110) surface is noncovalent. This remains true at both zero and room temperature. Thermal atomic fluctuations, such as motions of TiO_2 surface oxygens and acoustic modes of Au_{20}, influence energies and wave functions of the electronic states. The energy of the surface plasmon is affected primarily by the acoustic modes of Au_{20}, which alter the shape and size of the nanoparticle. The plasmon wave function is also influenced by the dipolar Ti−O bond vibrations, through the electrostatic interaction. TiO_2 states and the Au_{20} HOMO are subject to higher frequency phonons than the plasmon.

The strong optical response of surface plasmon, rapid charge separation at the Au−TiO_2 interface, and a significantly slower electron−hole recombination provide the fundamental basis for utilization of plasmon-sensitized TiO_2 as an excellent photovoltaic material and a visible-light photocatalyst.

■ ASSOCIATED CONTENT

Supporting Information

DOS of the isolated Au_{20} particle and TiO_2 slab, absorption spectrum of the Au−TiO_2 system, and plasmonic excitation densities of the ideal system and the systems with O and Au vacancies computed using the hybrid HSE06 DFT functional. This material is available free of charge via Internet at http://pubs.acs.org.

■ AUTHOR INFORMATION

Corresponding Author

oleg.prezhdo@rochester.edu

Notes

The authors declare no competing financial interest.

■ ACKNOWLEDGMENTS

R.L. thanks the Science Foundation Ireland (SFI) SIRG Program (grant no. 11/SIRG/E2172), UCD Seed Funding SF895, and the Irish Center for High End Computing for the provision of computational resources. O.V.P. acknowledges grant CHE-1300118 from the U.S. National Science Foundation.

■ REFERENCES

(1) Subramanian, V.; Wolf, E. E.; Kamat, P. V. *J. Am. Chem. Soc.* **2004**, *126*, 4943.
(2) Schwartz, V.; Mullins, D. R.; Yan, W.; Chen, B.; Dai, S.; Overbury, S. H. *J. Phys. Chem. B* **2004**, *108*, 15782.
(3) Chen, M. S.; Goodman, D. W. *Catal. Today* **2006**, *111*, 22.
(4) Matthey, D.; Wang, J. G.; Wendt, S.; Matthiesen, J.; Schaub, R.; Lægsgaard, E.; Hammer, B.; Besenbacher, F. *Science* **2007**, *315*, 1692.
(5) Zhu, H. M.; Song, N. H.; Lv, H. J.; Hill, C. L.; Lian, T. Q. *J. Am. Chem. Soc.* **2012**, *134*, 11701.
(6) Wang, L.; Wang, H.; Hapala, P.; Zhu, L. F.; Ren, L. M.; Meng, X. J.; Lewis, J. P.; Xiao, F. S. *J. Catal.* **2011**, *281*, 30.
(7) Akimov, A. V.; Muckerman, J. T.; Prezhdo, O. V. *J. Am. Chem. Soc.* **2013**, *135*, 8682.
(8) Park, J. B.; Graciani, J.; Evans, J.; Stacchiola, D.; Senanayake, S. D.; Barrio, L.; Liu, P.; Sanz, J. F.; Hrbek, J.; Rodriguez, J. A. *J. Am. Chem. Soc.* **2009**, *132*, 356.
(9) Qi, J.; Dang, X.; Hammond, P. T.; Belcher, A. M. *ACS Nano* **2011**, *5*, 7108.
(10) Brown, G. E.; Henrich, V. E.; Casey, W. H.; Clark, D. L.; Eggleston, C.; Felmy, A.; Goodman, D. W.; Grätzel, M.; Maciel, G.; McCarthy, M. I.; Nealson, K. H.; Sverjensky, D. A.; Toney, M. F.; Zachara, J. M. *Chem. Rev.* **1998**, *99*, 77.
(11) Furube, A.; Du, L.; Hara, K.; Katoh, R.; Tachiya, M. *J. Am. Chem. Soc.* **2007**, *129*, 14852.
(12) Tian, Y.; Tatsuma, T. *J. Am. Chem. Soc.* **2005**, *127*, 7632.
(13) Vazhappilly, T.; Kilin, D. S.; Micha, D. A. *J. Phys. Chem. C* **2012**, *116*, 25525.
(14) Kilin, D. S.; Micha, D. A. *J. Phys. Chem. C* **2011**, *115*, 770.
(15) Wu, K. F.; Zhu, H. M.; Liu, Z.; Rodriguez-Cordoba, W.; Lian, T. Q. *J. Am. Chem. Soc.* **2012**, *134*, 10337.
(16) Chen, Y.-S.; Choi, H.; Kamat, P. V. *J. Am. Chem. Soc.* **2013**, *135*, 8822.
(17) Mayer, K. M.; Lee, S.; Liao, H.; Rostro, B. C.; Fuentes, A.; Scully, P. T.; Nehl, C. L.; Hafner, J. H. *ACS Nano* **2008**, *2*, 687.
(18) Pozzi, E. A.; Sonntag, M. D.; Jiang, N.; Klingsporn, J. M.; Hersam, M. C.; Van Duyne, R. P. *ACS Nano* **2013**, *7*, 885.
(19) Reineck, P.; Gomez, D.; Ng, S. H.; Karg, M.; Bell, T.; Mulvaney, P.; Bach, U. *ACS Nano* **2013**, *7*, 6636.
(20) Hartland, G. V. *Chem. Rev.* **2011**, *111*, 3858.
(21) Jensen, L.; Aikens, C. M.; Schatz, G. C. *Chem. Soc. Rev.* **2008**, *37*, 1061.
(22) Provorse, M. R.; Aikens, C. M. *J. Am. Chem. Soc.* **2010**, *132*, 1302.
(23) Murphy, S.; Huang, L. B.; Kamat, P. V. *J. Phys. Chem. C* **2013**, *117*, 4740.
(24) Ghosh, S. K.; Pal, T. *Chem. Rev.* **2007**, *107*, 4797.
(25) Gobin, A. M.; Lee, M. H.; Halas, N. J.; James, W. D.; Drezek, R. A.; West, J. L. *Nano Lett.* **2007**, *7*, 1929.
(26) Murphy, C. J.; Gole, A. M.; Stone, J. W.; Sisco, P. N.; Alkilany, A. M.; Goldsmith, E. C.; Baxter, S. C. *Acc. Chem. Res.* **2008**, *41*, 1721.
(27) Carr, J. A.; Wang, H.; Abraham, A.; Gullion, T.; Lewis, J. P. *J. Phys. Chem. C* **2012**, *116*, 25816.
(28) Min, C.; Wang, P.; Chen, C.; Deng, Y.; Lu, Y.; Ming, H.; Ning, T.; Zhou, Y.; Yang, G. *Opt. Lett.* **2008**, *33*, 869.
(29) Le, F.; Brandl, D. W.; Urzhumov, Y. A.; Wang, H.; Kundu, J.; Halas, N. J.; Aizpurua, J.; Nordlander, P. *ACS Nano* **2008**, *2*, 707.
(30) Nahm, C.; Choi, H.; Kim, J.; Jung, D.-R.; Kim, C.; Moon, J.; Lee, B.; Park, B. *Appl. Phys. Lett.* **2011**, *99*, 253107.
(31) Mubeen, S.; Hernandez-Sosa, G.; Moses, D.; Lee, J.; Moskovits, M. *Nano Lett.* **2011**, *11*, 5548.
(32) Han, Y.; Tretiak, S.; Kilin, D. *Mol. Phys.* **2013**, *112*, 474.
(33) Craig, C. F.; Duncan, W. R.; Prezhdo, O. V. *Phys. Rev. Lett.* **2005**, *95*, 163001.
(34) Habenicht, B. F.; Prezhdo, O. V. *Phys. Rev. Lett.* **2008**, *100*, 197402.
(35) Jaeger, H. M.; Fischer, S.; Prezhdo, O. V. *J. Chem. Phys.* **2012**, *137*, 22A545.

(36) Bigelow, N. W.; Vaschillo, A.; Iberi, V.; Camden, J. P.; Masiello, D. J. *ACS Nano* **2012**, *6*, 7497.
(37) Kilina, S. V.; Kilin, D. S.; Prezhdo, O. V. *ACS Nano* **2008**, *3*, 93.
(38) Tully, J. C. *J. Chem. Phys.* **1990**, *93*, 1061.
(39) Hammes-Schiffer, S.; Tully, J. C. *J. Chem. Phys.* **1994**, *101*, 4657.
(40) Parandekar, P. V.; Tully, J. C. *J. Chem. Phys.* **2005**, *122*, 094102.
(41) Tretiak, S.; Igumenshchev, K.; Chernyak, V. *Phys. Rev. B* **2005**, *71*, 033201.
(42) Baer, R.; Neuhauser, D. *J. Chem. Phys.* **2004**, *121*, 9803.
(43) Chapman, C. T.; Liang, W.; Li, X. S. *J. Phys. Chem. Lett.* **2011**, *2*, 1189.
(44) Kohn, W.; Sham, L. J. *Phys. Rev.* **1965**, *140*, A1133.
(45) Cramer, C. J.; Truhlar, D. G. *Phys. Chem. Chem. Phys.* **2009**, *11*, 10757−10816.
(46) Jasper, A. W.; Nangia, S.; Zhu, C.; Truhlar, D. G. *Acc. Chem. Res.* **2005**, *39*, 101.
(47) Long, R.; Prezhdo, O. V. *J. Am. Chem. Soc.* **2011**, *133*, 19240.
(48) Fischer, S. A.; Duncan, W. R.; Prezhdo, O. V. *J. Am. Chem. Soc.* **2009**, *131*, 15483.
(49) Duncan, W. R.; Prezhdo, O. V. *J. Phys. Chem. B* **2005**, *109*, 17998.
(50) Bao, H.; Habenicht, B. F.; Prezhdo, O. V.; Ruan, X. *Phys. Rev. B* **2009**, *79*, 235306.
(51) Long, R.; English, N. J.; Prezhdo, O. V. *J. Am. Chem. Soc.* **2012**, *134*, 14238.
(52) Duncan, W. R.; Craig, C. F.; Prezhdo, O. V. *J. Am. Chem. Soc.* **2007**, *129*, 8528.
(53) Akimov, A. V.; Neukirch, A. J.; Prezhdo, O. V. *Chem. Rev.* **2013**, *113*, 4496.
(54) Sousa, C.; Tosoni, S.; Illas, F. *Chem. Rev.* **2012**, *113*, 4456.
(55) Prezhdo, O. V. *J. Chem. Phys.* **1999**, *111*, 8366.
(56) Isborn, C. M.; Li, X.; Tully, J. C. *J. Chem. Phys.* **2007**, *126*, 134307.
(57) Prezhdo, O. V.; Rossky, P. J. *J. Chem. Phys.* **1997**, *107*, 5863.
(58) Bittner, E. R.; Rossky, P. J. *J. Chem. Phys.* **1995**, *103*, 8130.
(59) Mukamel, S. In *Principles of Nonlinear Optical Spectroscopy*; Oxford University Press: New York, 1995.
(60) Habenicht, B. F.; Kamisaka, H.; Yamashita, K.; Prezhdo, O. V. *Nano Lett.* **2007**, *7*, 3260.
(61) Habenicht, B. F.; Kalugin, O. N.; Prezhdo, O. V. *Nano Lett.* **2008**, *8*, 2510.
(62) Ulrike, D. *Surf. Sci. Rep.* **2003**, *48*, 53.
(63) Li, J.; Li, X.; Zhai, H.-J.; Wang, L.-S. *Science* **2003**, *299*, 864.
(64) Gruene, P.; Rayner, D. M.; Redlich, B.; van der Meer, A. F. G.; Lyon, J. T.; Meijer, G.; Fielicke, A. *Science* **2008**, *321*, 674.
(65) Kresse, G.; Furthmüller, J. *Phys. Rev. B* **1996**, *54*, 11169.
(66) Perdew, J. P.; Burke, K.; Ernzerhof, M. *Phys. Rev. Lett.* **1996**, *77*, 3865.
(67) Dudarev, S. L.; Botton, G. A.; Savrasov, S. Y.; Humphreys, C. J.; Sutton, A. P. *Phys. Rev. B* **1998**, *57*, 1505.
(68) Du, A.; Ng, Y. H.; Bell, N. J.; Zhu, Z.; Amal, R.; Smith, S. C. *J. Phys. Chem. Lett.* **2011**, *2*, 894.
(69) Nelson, T. R.; Prezhdo, O. V. *J. Am. Chem. Soc.* **2013**, *135*, 3702.
(70) Kilina, S.; Velizhanin, K. A.; Ivanov, S.; Prezhdo, O. V.; Tretiak, S. *ACS Nano* **2012**, *6*, 6515.
(71) Chaban, V. V.; Prezhdo, V. V.; Prezhdo, O. V. *J. Phys. Chem. Lett.* **2012**, *4*, 1.
(72) Kamisaka, H.; Kilina, S. V.; Yamashita, K.; Prezhdo, O. V. *Nano Lett.* **2006**, *6*, 2295.
(73) Madrid, A. B.; Hyeon-Deuk, K.; Habenicht, B. F.; Prezhdo, O. V. *ACS Nano* **2009**, *3*, 2487.
(74) Blobner, F.; Coto, P. B.; Allegretti, F.; Bockstedte, M.; Rubio-Pons, O.; Wang, H. B.; Allara, D. L.; Zharnikov, M.; Thoss, M.; Feulner, P. *J. Phys. Chem. Lett.* **2012**, *3*, 436.
(75) Rego, L. G. C.; Batista, V. S. *J. Am. Chem. Soc.* **2003**, *125*, 7989.
(76) Guo, D.; Knight, T. E.; McCusker, J. K. *Science* **2011**, *334*, 1684.
(77) Stier, W.; Duncan, W. R.; Prezhdo, O. V. *Adv. Mater.* **2004**, *16*, 240.
(78) Stier, W.; Prezhdo, O. V. *J. Phys. Chem. B* **2002**, *106*, 8047.
(79) Duncan, W. R.; Prezhdo, O. V. *J. Am. Chem. Soc.* **2008**, *130*, 9756.
(80) Duncan, W. R.; Stier, W. M.; Prezhdo, O. V. *J. Am. Chem. Soc.* **2005**, *127*, 7941.
(81) Choi, H.; Chen, W. T.; Kamat, P. V. *ACS Nano* **2012**, *6*, 4418.
(82) Chen, W.-T.; Hsu, Y.-J.; Kamat, P. V. *J. Phys. Chem. Lett.* **2012**, *3*, 2493.
(83) Cushing, S. K.; Li, J.; Meng, F.; Senty, T. R.; Suri, S.; Zhi, M.; Li, M.; Bristow, A. D.; Wu, N. *J. Am. Chem. Soc.* **2012**, *134*, 15033.
(84) Miller, W. H.; George, T. F. *J. Chem. Phys.* **1972**, *56*, 16.
(85) Guo, Z.; Habenicht, B. F.; Liang, W.-Z.; Prezhdo, O. V. *Phys. Rev. B* **2010**, *81*, 125415.
(86) Neukirch, A. J.; Guo, Z.; Prezhdo, O. V. *J. Phys. Chem. C* **2012**, *116*, 15034.
(87) Molina, B. S.; Calles., J. R. *Rev. Mex. Fis.* **2008**, *54*, 5.
(88) Baumard, J.-F.; Gervais, F. *Phys. Rev. B* **1977**, *15*, 2316.
(89) Lehmann, J.; Merschdorf, M.; Pfeiffer, W.; Thon, A.; Voll, S.; Gerber, G. *Phys. Rev. Lett.* **2000**, *85*, 2921.
(90) Krukau, A. V.; Vydrov, O. A.; Izmaylov, A. F.; Scuseria, G. E. *J. Chem. Phys.* **2006**, *125*, 224106.
(91) Long, R.; English, N. J.; Prezhdo, O. V. *J. Am. Chem. Soc.* **2013**, *135*, 18892.
(92) Gong, X.-Q.; Selloni, A.; Dulub, O.; Jacobson, P.; Diebold, U. *J. Am. Chem. Soc.* **2007**, *130*, 370.
(93) Liu, M.; Pelton, M.; Guyot-Sionnest, P. *Phys. Rev. B* **2009**, *79*, 035418.
(94) Link, S.; El-Sayed, M. A. *J. Phys. Chem. B* **1999**, *103*, 4212.
(95) Swamy, V. *Phys. Rev. B* **2008**, *77*, 195414.
(96) Wang, Z.; Yang, C.; Lin, T.; Yin, H.; Chen, P.; Wan, D.; Xu, F.; Huang, F.; Lin, J.; Xie, X.; Jiang, M. *Adv. Funct. Mater.* **2013**, *23*, 5444.